



Power production locality of bluff body flutter mills using fully coupled 2D direct numerical simulation

J.M. Kuhl, P.E. Desjardin*

Department of Mechanical and Aerospace Engineering, University at Buffalo, the State University of New York Buffalo, NY 14260-4400, USA

ARTICLE INFO

Article history:

Received 11 July 2011

Accepted 1 December 2011

Available online 4 January 2012

Keywords:

Flutter

Fluid structure interaction

Flow induced vibration

ABSTRACT

Two-dimensional, fully coupled direct numerical simulations (DNS) are conducted to examine the local energy dynamics of a flexible cantilevered plate in the wake of a two-dimensional circular cylinder. The motion of the cantilevered plate is described using a finite element formulation and a fully compressible, finite volume Navier Stokes solver is used to compute the flow field. A sharp interface level set method is employed in conjunction with a ghost fluid method to describe the immersed boundaries of the bluff body and flexible plate. DNS is first conducted to validate the numerical methodology and compared with previous studies of flexible cantilevered plates and flow over bluff bodies; excellent agreement with previous results is observed. A newly defined power production/loss geometry metric is introduced based on surface curvature and plate velocity. The metric is found to be useful for determining which sections of the plate will produce energy based on curvature and deflection rate. Scatter plots and probability measures are presented showing a high correlation between the direction of energy transfer (*i.e.*, to or from the plate) and the sign of the newly defined curvature-deflection-rate metric. The findings from this study suggest that a simple local geometry/kinematic based metric can be devised to aid in the development and design of flexible wind energy harvesting flutter mills.

© 2011 Elsevier Ltd. All rights reserved.

1. Introduction

With the advent of technology that facilitates real-time monitoring and control in a wide range of applications, a need has emerged for a simple, reliable and renewable way to power these devices. Remote sensing is commonplace in applications ranging from military to environment monitoring, to traffic control (Pennington et al., 2009) with batteries as the primary power source. Considering today's increasing emphasis on environmentally aware practices and renewable power, it is highly desirable to develop alternatives to battery power. One alternative energy solution for small, remote sensing applications which has received considerable attention as of late are flutter energy harvesters which are capable of extracting small amounts of power from fluid flowing at speeds well below what is required for a typical horizontal-axis wind turbine (HAWT).

Wind-energy extraction through transverse motion was first suggested as a large-scale alternative to the HAWT in the form of a pitching and plunging rigid wing used to transfer energy of an airflow into rotational motion of a shaft (Ly and Chasteau, 1981; McKinney and DeLaurier, 1981). The "Energy Harvesting Eel" (Taylor et al., 2001) was proposed as a small,

* Corresponding author. Tel.: +1 716 645 1467.

E-mail address: ped3@buffalo.edu (P.E. Desjardin).

piezoelectric plate in the wake of a bluff body, capable of extracting energy from flowing water as a means to power submerged, remote sensors. Humdinger Wind Energy, LLC (2008) has developed and is marketing the Windbelt™ as a scalable way to harvest energy from air flows through vibration of flexible membranes using novel linear actuators. The Windbelt™ can take the form of small microBelts™ for low-power applications or large arrays of Windcells™ intended as an alternative to traditional turbines. The flutter-mill (Tang et al., 2009) takes advantage of the instability inherent to cantilevered plates in axial flow to extract power from wind using a flexible plate with embedded conductors between two magnetic panels.

Closely related to the study of flutter energy harvesters is the classical problem of vibration of a cantilevered plate in axial flow. This problem was first discussed by Rayleigh (1878) who showed that a massless, infinite surface separating two parallel streams was always unstable, a result of his analysis of the stability of jets. The natural extension of the work of Lord Rayleigh is the theoretical analysis of Kornecki et al. (1976) which showed the existence of a critical flow velocity above which plates of finite chord and infinite span are unstable. Even more recently, theoretical approaches by Guo and Paidoussis (2000a,b) for plates in channel flow and Eloy et al. (2007) for plates in an infinite domain have shown that for finite span plates, the critical velocity is a decreasing function of the ratio of plate length to plate span. Recent work has characterized the critical velocity of finite-chord plates as a decreasing function of plate length and an increasing function of plate stiffness (Howell et al., 2009). A consistent finding in studies of plate flutter is underestimation of the critical velocity of numerical studies compared to experimental studies. Doaré et al. (2011) addressed this discrepancy through a theoretical investigation and found that slow convergence of the critical velocity to the two-dimensional limit with the ratio of channel width to plate span makes experimental reproduction of a two-dimensional scenario impossible.

For the case of cantilevered plates in axial flow, the fluid loading can be characterized as the combination of the unsteady pressure loading from the plate's wake, and the quasi-steady lift resulting from the flow around the instantaneous deformed shape of the plate. The relative influence of the steady and quasi-steady portions of the lift were analyzed theoretically by Huang (1995) using Theodorsen's theory to compute the lift and a one-dimensional linear beam equation to represent the plate. It was shown that for an isolated plate in uniform axial flow, energy is transferred to the plate by the quasi-steady portion of the lift while plate energy is dissipated by the unsteady wake. Above the critical flow speed, the net rate of energy transfer to the plate by the quasi-steady pressure loading is significantly larger than the rate of plate energy dissipated in the unsteady wake resulting in an overall increase in total plate energy with time. Recent numerical studies have shown an agreement with the theoretical work of Huang regarding the effect of the unsteady wake on the plate dynamics. Howell et al. (2009) used a linearized boundary-element-method (BEM) for the flow solution and a linear one-dimensional plate equation to explore the stability of the fluid–structure system using both time-stepping and state space methods. For short plates, the wake was found to increase the critical velocity with instability resulting from mid-plate fluid-to-plate energy transfer and plate-to-fluid energy transfer occurring over the trailing quarter of the plate. For long plates, energy equilibrium was shown in the downstream-most quarter and the wake was shown to have a lesser effect on the stability. More recently, Howell et al. (2011) has demonstrated that the critical flow speed can be controlled by inhomogeneous placement of mass along the length of the plate.

Good agreement was found with the results of Howell et al. (2009) in the careful study of the wake's influence by Tang and Paidoussis (2008) who used a nonlinear, one-dimensional plate model including axial deformation and Kelvin–Voigt type damping in combination with a lumped vortex model of the flow solution. Higher mode (frequency) vibrations of longer plates at the stability limit were found to reduce the effect of vibration-induced flow momentum on the overall plate forcing because of the smaller ratio of wake velocities to the plate deflection rate. A non-linear plate model was also used in the work of Yadykin et al. (2001), with the fluid loading calculated using slender wing theory. Limit cycle behavior was demonstrated above a critical flow speed and a dependence of plate behavior on initial condition was observed. Large initial deflections, on the order of 100 times the plate thickness, were shown to initiate limit-cycle behavior while the same flow conditions resulted in decaying amplitude vibrations when the initial deflection was on the order of the plate thickness. Initial condition dependent behavior has also been observed experimentally. When the flow speed is increased above the critical velocity and incrementally reduced to a sub-critical flow speed, a hysteresis loop is formed, *i.e.*, flutter ceases at a flow velocity below that at which flutter was initiated. The cause of the flutter hysteresis loop has been discussed and explored, inconclusively, in much of the literature relating to the subject of cantilevered plates in axial flow (Tang and Paidoussis, 2007; Tang et al., 2009).

The contribution of the present work is to use a newly developed ghost fluid method (McGurn et al., *in review*) to explore the local energy transfer to flexible cantilevered plates with a bluff body object upstream. It will be shown that the location at which energy is imparted to the plate is well correlated with the product of the local curvature and deflection rate. When the plate is convex in the direction of the deflection rate, energy is transferred from the fluid to the plate. Several cases are explored to investigate the generality of this observation as quantified using a probability correlation. The remainder of this study starts with a summary of the plate and flow models in Sections 2.1 and 2.2, respectively. Numerical methodologies used to solve the plate and fluid models are discussed in Section 3 with a note on the stability of the coupled fluid–structure algorithm. Results are presented in Section 4.1 starting with several validation problems to test the fluid, plate and coupled models. A parametric study of the effects of D/L is conducted and the locality of power generation discussed. Finally, conclusions are summarized from this study.

2. Mathematical formulation

The problem of interest is shown in Fig. 1 consisting of a flexible plate of length L , thickness h , and infinite span, which is positioned downstream of a leading bluff body cylinder of diameter D . The plate is assumed to be perfectly clamped where it attaches to the cylinder and the trailing edge is free. The cylinder is assumed perfectly rigid and provides a mechanism for the generation of vortices via a Karman vortex street. The plate is described using time dependent one-dimensional Euler–Bernoulli beam theory. The flow is modeled using the Navier–Stokes equations. Further details of these models are provided in the following subsections.

2.1. Fluid dynamics

A wide variety of numerical approaches with varying complexity have been employed in previous studies of cantilevered plates in axial flow. In the vast majority of studies, the flow solver formulation is based on potential flow theory with viscous effects accounted for through the Kutta condition at the trailing edge of the plate. To the authors' knowledge, the first study to describe the flow field using the equations of a fully compressible, viscous fluid is the study of Watanabe et al. (2002). Though incompressible, viscous flow solutions have been presented since then by Zhu and Peskin (2002) and Lucey and Balint (2005). In the present study, a fully viscous flow solution is used to explore the dynamics of the cantilevered plate in the vortical wake of a two-dimensional cylinder.

For this study, the flow field is modeled using the mass, momentum (Navier–Stokes) and energy equations for a fully compressible fluid,

$$\frac{\partial \rho_f}{\partial t} + \nabla \cdot (\rho_f \mathbf{u}) = 0, \quad (1a)$$

$$\frac{\partial (\rho_f \mathbf{u})}{\partial t} + \nabla \cdot (\rho_f \mathbf{u} \mathbf{u} + p) = \nabla \cdot \tilde{\boldsymbol{\tau}}, \quad (1b)$$

$$\frac{\partial (\rho_f E)}{\partial t} + \nabla \cdot (\rho_f \mathbf{u} H) = \nabla \cdot (\mathbf{u} \cdot \tilde{\boldsymbol{\tau}}) - \nabla \cdot \mathbf{q}, \quad (1c)$$

where ρ_f is the density of the fluid, \mathbf{u} is the fluid velocity, p is the fluid pressure, $E (= e + \frac{1}{2} \mathbf{u} \cdot \mathbf{u})$ is the total energy and $H (= h + \frac{1}{2} \mathbf{u} \cdot \mathbf{u})$ is the total enthalpy. The viscous stress tensor, $\tilde{\boldsymbol{\tau}}$, and heat conduction, \mathbf{q} , are modeled using Newton's and Fourier's Laws, respectively:

$$\tilde{\boldsymbol{\tau}} = \mu \left[-\frac{2}{3} \nabla \cdot \mathbf{u} + (\nabla \mathbf{u} + (\nabla \mathbf{u})^T) \right], \quad (2a)$$

$$\mathbf{q} = -k \nabla T, \quad (2b)$$

where the fluid viscosity, μ , and conductivity, k , are set to that of air at standard temperature and pressure. Zero penetration and no slip conditions are imposed at the fluid–solid interface. The normal derivative of the fluid pressure at the interface is set using the tangential velocity and the local fluid acceleration from the plate motion. Heat generation as a result of the viscous damping of the plate material is assumed to be negligible, therefore the plate is assumed adiabatic, thus giving

$$\mathbf{u} \cdot \hat{\mathbf{n}} = \dot{v}, \quad (3a)$$

$$\mathbf{u} \cdot \hat{\mathbf{t}} = 0, \quad (3b)$$

$$\frac{\partial p}{\partial \mathbf{n}} = \rho_f \left[\frac{(\mathbf{u} \cdot \hat{\mathbf{t}})^2}{R} - \ddot{v} \right], \quad (3c)$$

$$\frac{\partial T}{\partial \mathbf{n}} = 0, \quad (3d)$$

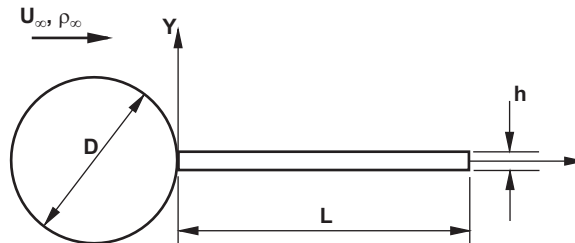


Fig. 1. Sketch of bluff body flutter mill model configuration.

where T is the temperature and \ddot{v} is the plate acceleration and \dot{v} is the instantaneous velocity of the plate. The unit vectors, \hat{n} and \hat{t} , are the interface outward facing normal, i.e., pointing from solid to fluid, and tangential, respectively, $R(= 1/(\nabla \cdot \hat{n}))$ is the radius of curvature.

2.2. Structural dynamics

Many studies, including the present, use Euler–Bernoulli theory of thin beams (plates) where the deflection is assumed to be on the order of the plate thickness and one-dimensional in the transverse direction. The major simplification of Euler–Bernoulli beam theory is that the deformation is assumed to occur as a result of bending only with shear deformation assumed negligible; the effects of fluid drag induced tension are also neglected. More sophisticated nonlinear models of the plate dynamics have been introduced following the work of Semler et al. (1994) and used by Yadykin et al. (2001) and Tang and Paidoussis (2007, 2008) and Tang et al. (2009). It is also worth noting that to date, no mathematical models accounting for the effects of three-dimensional flow and deformation have been used in numerical studies.

The governing equation for the unsteady displacement $v(x,t)$, per unit width, of a cantilevered plate under Euler–Bernoulli thin beam theory is (Inman, 1996)

$$\rho_p h \ddot{v}(x,t) + C \dot{v}(x,t) + B v''''(x,t) = \Delta p(x,t). \tag{4}$$

The boundary conditions for the plate are those of vanishing deflection and slope at the clamped leading edge, $v(0,t) = 0$ m, $v'(0,t) = 0$ and zero bending moment and shear force at the trailing edge $v''(L,t) = 0$ m⁻¹, $v'''(L,t) = 0$ m⁻². Differentiation with respect to time, and the axial direction of the undeformed plate are represented with the shorthand ($\dot{\cdot}$) and (\prime), respectively. The material properties and geometry are assumed constant with $B = Eh^3/12(1-\nu^2)$, where E denotes the plate’s elastic modulus and ν Poisson’s ratio. The plate density is ρ_p , the velocity proportional dissipation term C is introduced as a model of the visco-elastic response of the material. The fluid loading is represented by the vertical component of the difference of the pressure on the top $p_T(x,t)$, and bottom $p_B(x,t)$, of the plate:

$$\Delta p(x,t) = (p_B(x,t) - p_T(x,t)) \cos(\text{atan}(v'(x,t))). \tag{5}$$

2.2.1. Energy analysis

Following the work of Lucey and Balint (2005), the governing equation for the evolution of the total plate energy per unit width may be derived by multiplying Eq. (4) by the deflection rate $\dot{v}(x,t)$, and integrating over the length of the plate:

$$\frac{d}{dt} \left(\underbrace{\frac{1}{2} \rho_p h \int_0^L \dot{v}^2 dx}_{E_k} + \underbrace{\frac{1}{2} B \int_0^L (v'')^2 dx}_{E_s} \right) = \int_0^L \underbrace{\Delta p \dot{v} dx}_{\dot{W}} - C \underbrace{\int_0^L \dot{v}^2 dx}_{\dot{D}_v}. \tag{6}$$

The kinetic and strain energies are E_k and E_s , respectively and E_t is the total energy. The instantaneous local power of the fluid–structure interaction is $\dot{W}(t,x)$, and the rate of energy dissipation through viscous damping of the plate model is $\dot{D}_v(t)$. As will be presented in the results, it is also instructive to look at the total work done by fluid pressure on an element of the structure over a time interval from 0 s to t_e , which is calculated as $W(t_e,x) = \int_0^{t_e} \dot{W} dt$.

3. Numerical methods

Partitioned approaches for numerically solving coupled fluid–structure problems are popular due to the flexibility that they afford with respect to discretization, methods of solution and parallel decomposition. For this study, a one-dimensional finite element solver is used to compute the structural dynamics and a two-dimensional, block-structure, finite-volume Navier–Stokes code is used to compute the flow field. The only requirement of each solver is that each is able to provide the coupling variables to the other at a dynamically computed coupling interval Δt_{coup} . Specifically, the structural solver provides the position, velocity and acceleration of the plate to the flow solver and the flow solver provides the local pressure for the structural solution.

Because of the Courant–Friedrichs–Lewy (CFL) time step restrictions for the CFD solver, several intermediate time steps are required by the flow solver over the coupling time interval. The plate solution, however, is solved implicitly and therefore does not require intermediate time stepping to maintain numerical stability. As discussed by Borazjani et al. (2008), a loose coupled approach, where the coupling variables are determined explicitly, works well when the mass ratio $L^* = \rho_f L / \rho_p h$ is low. At high mass ratios, however, numerical instability is observed and a more robust strongly coupled method is required; similar characteristics of the numerical instability are found in this study. The strong coupled approach consists of Gauss–Seidel type sub-iterations to compute the pressure loading in a semi-implicit manner. For very large mass ratios, it is found necessary to incorporate the Aitken acceleration scheme into the sub-iterations to achieve fast convergence, consistent with the findings of Borazjani et al. (2008).

3.1. Fluid dynamics

The flow solver used is based on a finite volume formulation using the AUSM family of flux splitting schemes (Liou, 1996, 2006). Fluxes at the cell faces are interpolated using second order upwind biased stencils (Li, 1997). A constant velocity inlet is imposed at the lower vertical boundary; all other boundaries are characteristic based open boundaries which allow vorticity to pass out of the domain. The equations are integrated in time using a second order Runge–Kutta method with Ralston weights. A block-structured domain decomposition is employed to partition the solution integration over multiple processors. A region communicates with neighboring blocks through a ghost cell (not to be confused with ghost fluid cells) strategy using a native Java version of the message passing interface (MPI) (Shafi and Manzoor, 2009). Further details on the flow numerics can be found in Desjardin et al. (2004).

The plate geometry is accounted for in the flow solver using a newly developed sharp interface level set based ghost fluid method (McGurn et al., in review). In this approach, a narrow range of ghost fluid cells are defined near the boundary of the fluid–solid interface. The means of populating the properties of the ghost fluid cells and interface description distinguishes one embedded interface methodology from another. Several variants of ghost fluid cell updates have been tailored for the use of level set interface descriptions for both incompressible (Osher and Fedkiw, 2003) and compressible (Arienti et al., 2003; Fedkiw, 2002; Fedkiw et al., 1999; Wag et al., 2008; Xu et al., 1997) flows and are problem dependent. The level set function is updated after each coupling interval using a two-dimensional surface mesh, discussed further in Section 3.2.

To enforce boundary conditions on the flow solver at fluid–structure interfaces, a reflection method following that of Ye et al. (1999) is used. A band of ghost fluid nodes are identified along the fluid–solid interface inside the solid. For a ghost fluid node at \mathbf{x}_G , the mirror image across the interface \mathbf{x} is determined as

$$\mathbf{x} = \mathbf{x}_G + 2\gamma_g(\mathbf{x}_G, t)\hat{n}_g, \quad (7)$$

where \hat{n}_g is the unit vector normal to the interface from \mathbf{x}_G . After \mathbf{x} is determined, Newton interpolating polynomials are used to compute the appropriate constraints to impose at the intersection of the line $\mathbf{x}_G - \mathbf{x}$ and the interface, i.e., at $\mathbf{x}_I = \mathbf{x} + \gamma_g(\mathbf{x}_G, t)\hat{n}_g$. To determine the flow conditions at \mathbf{x}_G which will yield the desired constraints at \mathbf{x}_I , a 4×4 matrix must be inverted. For computational efficiency, the matrix inversions for Neumann and Dirichlet type boundary conditions at each ghost fluid node are precomputed and stored each time once the Lagrangian mesh is updated, the inverse matrices can then be used repeatedly to impose the boundary conditions, Eq. (1), until the Lagrangian mesh is again updated, preventing unnecessary repetitive matrix inversions. For a more detailed description of immersed boundary methods see McGurn et al. (in review), Sambasivan and UdayKumar (2009), and Ye et al. (1999).

3.2. Structural dynamics

The plate model is solved using finite elements (FE) in a standard Galerkin formulation with Hermite cubic polynomial basis functions (Reddy, 1993). In this approach, the displacement field at time level n , corresponding to time t_n , is defined in terms of four basis functions, $v(x, t_n) = \sum_{i=1}^4 \psi_i^n(t_n)\phi_i^e(x)$, where $\phi_i^e(x)$ is the basis function of element e and ψ_i^n are coefficients associated with the instantaneous displacement and its derivative at the left and right boundaries of the element, i.e., $\psi_1^n = v(x_e, t_n)$, $\psi_2^n = dv/dx|_{x=x_e, t=t_n}$, $\psi_3^n = v(x_{e+1}, t_n)$ and $\psi_4^n = dv/dx|_{x=x_{e+1}, t=t_n}$. Following a standard finite element derivation, the following semi-discrete system of equations results for each element:

$$[M^e]\{\ddot{\psi}^{n+1}\} + [C^e]\{\dot{\psi}^{n+1}\} + [K^e]\{\psi^{n+1}\} = \{F^e\}^{n+1}, \quad (8)$$

where $[M^e]$, $[C^e]$, $[K^e]$ are the mass, damping and stiffness matrices. The quantity $\{F^e\} = \{F_1^e, 0, F_3^e, 0\}$ where $F_i^e = \int \Delta p(x, t)\phi_i^e(x) dx$ is the pressure force loading from the fluid to the plate. The equations are integrated in time using the Newmark- β method with 160 nodes.

A surface mesh, extracted from the FE model, is needed to update the level set description of the plate in the CFD solver. A representation of the two-dimensional surface mesh is given in Fig. 2. Direct connectivity is enforced between nodes of

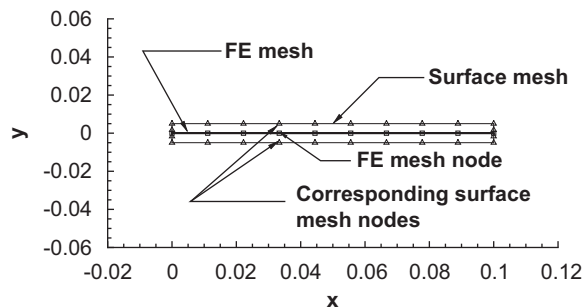


Fig. 2. Sketch of plate FE mesh and corresponding surface mesh.

the surface mesh and nodes of the FE mesh. The surface mesh position is updated using the displacement computed on the FE nodes at the beginning of every coupling interval. A complete description of the procedure used to initialize the level set from a surface mesh is given in McGurn et al. (in review).

To determine the fluid loading on the structure, a list of surface mesh nodes that contribute to the plate surface pressure are first identified. Pressure contributing nodes are all surface mesh nodes that are attached to at least one element whose normal is perpendicular to the axis of the plate when the plate is in the undeflected position. Bilinear interpolation in the CFD domain is used to determine the fluid pressure at each pressure contributing node of the surface mesh. The total pressure on each node of the FE mesh is then calculated as outlined in Eq. (5).

3.3. Time step selection

One of the challenges of solving the fully compressible Navier–Stokes equations with the plate model is the disparity between the timescales of the fluid and structural domains. When solving the Navier–Stokes equations explicitly, the Courant–Friedrichs and Lewy (CFL = $c\Delta t/\Delta x$) number is restricted to less than one, where c is the speed of the fastest acoustic wave. The structural solver is a fully implicit formulation which is unconditionally stable for the homogeneous equation. The computational cost of advancing both solutions subject to the smallest time step is prohibitive due to the large amount of information which must be processed and communicated during coupling. Instead, a minimum time step is enforced which ensures the physical processes are sampled at a sufficiently high frequency.

For the cases considered here, plate vibrations were found to be a combination of the first and second mode shapes. The timescale of the dominant flow structures is assumed to be based on the Strouhal number $St = f_{shed}D/U_\infty$ where f_{shed} is the frequency of vortex shedding and $St \approx 0.21$ for Reynolds number from 1000 to 10 000 (Smits, 1999). The minimum sample time step is then determined as

$$\Delta t_{physics} = \min\left(\frac{1}{n_s \omega_2}, \frac{D}{0.21 n_s U}\right), \tag{9}$$

where the frequency of second mode plate vibration ω_2 is calculated from the plate material properties and the second eigenvalue of the Euler–Bernoulli beam equation $\beta_2 = 4.694$:

$$\omega_2 = \frac{1}{2\pi} \left(\frac{\beta_2}{L}\right)^2 \sqrt{\frac{B}{\rho_p h}}. \tag{10}$$

In all simulations, the number of samples per cycle n_s , in Eq. (9), is 25.

From an accuracy standpoint, it is undesirable to allow the plate to move through a large number of CFD cells between coupling steps. Therefore, a discretization-based minimum time step, Eq. (11), is computed and enforced at each coupling interval with the scaling parameter $\varphi = 0.5$:

$$\Delta t_{coup} = \min\left(\Delta t_{physics}, \varphi \frac{\Delta x_{min}}{v_{max}}\right). \tag{11}$$

The minimum distance between adjacent nodes of the CFD mesh is Δx_{min} and v_{max} is the maximum local instantaneous velocity of the plate. In the simulations presented here, the stable time step of the CFD solver is on the order of $10^1 - 10^2$ times smaller than the calculated minimum coupling time step, consequently the CFD solution advances independently between coupling time steps.

4. Results

Several studies are conducted to validate the present numerical model and to explore the locations of fluid-to-plate and plate-to-fluid energy transfer. Validation studies of the fluid and structural solvers as stand alone entities are first presented. Quantitative and qualitative results are then used to show agreement between the coupled fluid–structure model of the present study and other published work. Finally, an analysis of the energy transfer as a function of instantaneous local plate conditions is presented demonstrating high correlation between local curvature, rate of deflection and fluid-to-plate energy transfer.

4.1. Validation

The first case considered is the motion of an undamped, unforced plate which is solved numerically by setting $\{C^e\}$ and $\{F^e\}$ equal to zero in Eq. (8). For the homogeneous, undamped case the analytical solution for the deflection can be expressed as

$$v(x,t) = \sum_{n=0}^{\infty} \chi_n(x) \tau_n(t),$$

$$\chi_n(x) = \cos(\beta_n x) + \cosh(\beta_n x) + \frac{\cos(\beta_n L) + \cosh(\beta_n L)}{\sin(\beta_n L) + \sinh(\beta_n L)} (\sinh(\beta_n x) - \sin(\beta_n x)),$$

$$\tau_n(t) = A_n \sin(\omega_n t) + B_n \cos(\omega_n t),$$

where $\chi_n(x)$ is the n th mode shape. The constants A_n and B_n are determined from the initial conditions and the eigenvalues β_n computed from the equation $\cosh(\beta_n L)\cos(\beta_n L) = 1$ (Inman, 1996). A plate initially displaced in the n th mode shape will vibrate with frequency $\omega_n = (1/2\pi)\beta_n^2 \sqrt{B/\rho_p h}$ and fully recover the initial condition over each cycle. To assess the fidelity of the FE solution, cases are run with the plate released from rest with an initial deflection profile equal to each of the first six mode shapes. The plate properties are $L=0.6$ m, $\rho_p h = 5.34$ kg/m³, $B = 10.22$ N m, $C = 0$ kg/m² s and the time step is $\Delta t = 1/(80\omega_n)$. Vibration frequencies in the first six mode shapes were computed by performing a discrete Fourier transform on the time history of the tip deflection of the plate. The percent error between the computed and analytical frequencies of vibration for modes one through six are 7.3×10^{-7} , 5.0×10^{-2} , 5.0×10^{-2} , 4.9×10^{-2} , 3.2×10^{-6} , $5.8 \times 10^{-6}\%$, respectively.

To assess the accuracy with which the flow solver can resolve unsteady flow features and pressure near fluid–solid interfaces, simulations of flow over a two-dimensional cylinder were investigated. Probes are placed along the upper half of the cylinder and monitored for pressure coefficient. The flow conditions are $U_\infty = 18.9$ m/s and $D=0.001$ m, resulting in a Reynolds number of 1000. Fig. 3(a) shows a comparison of the computed pressure coefficient with the DNS results of Tseng and Ferziger (2003) demonstrating strong correlation. At Reynolds numbers between 1000 and 10 000, the Strouhal

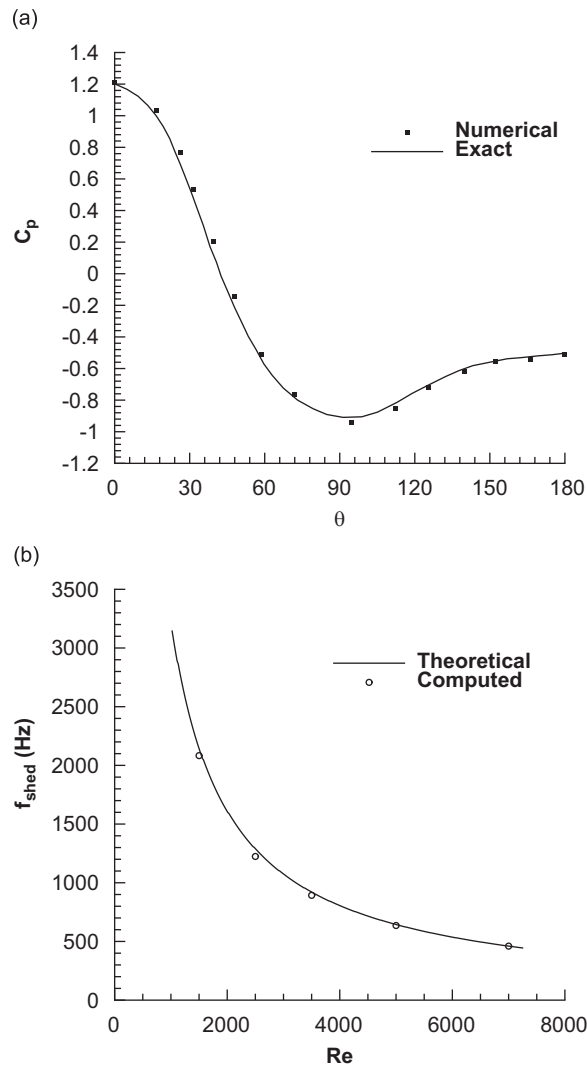


Fig. 3. Validation results showing (a) pressure coefficient and (b) vortex shedding frequency for flow over a cylinder.

number associated with vortex shedding is approximately constant at 0.21 (Smits, 1999). The vortex shedding frequency, f_{shed} , is calculated by taking the discrete Fourier transform of the cross-stream velocity at a distance D downstream of the cylinder. A comparison of the shedding frequency computed by the flow solver and from the Strouhal approximation is given in Fig. 3(b). The agreement is excellent.

To test the accuracy of the coupled simulations, two cases were run based on the numerical results of Howell et al. (2009) with the objective of showing consistency between the critical velocity of the present method and previously published studies. Howell et al. (2009) have shown that for an undamped plate $C^* \equiv (\rho_p h)^{3/2} / \rho_f^2 B^{1/2} = 0$, of mass ratio $L^* = \rho_f L / \rho_p h = 0.6$, the critical non-dimensional flow speed $U_c^* = 11.47$, where $U^* \equiv U_\infty (\rho_p h)^{3/2} / (\rho_f B^{1/2})$. Fig. 4 shows the evolution of plate tip deflection for $U^* = 5$ (sub-critical) and $U^* = 15$ (supercritical) as a function of the non-dimensional time, $T^* \equiv t(\rho_f^2 B^{1/2}) / (\rho_p h)^{5/2}$, using the non-dimensionalization suggested by Crighton and Oswell (1991). In both cases, second beam mode shape is used for the initial deflection profile with a tip deflection of $h/4$. For $U^* < U_c^*$, the plate tip deflection decays. For $U^* > U_c^*$ energy is transferred to the plate from the flow leading to flutter instability—consistent with the findings of Howell et al. (2009).

Fig. 5 shows the locality of energy transfer for the supercritical flow conditions of $U^* = 6.0$ and $L^* = 1.0$. The time history of work done in each quadrant of the plate (Q1–Q4) and the total are presented. The leading quadrant is Q1 and Q4 is at the trailing edge. Consistent with the findings of Howell et al. (2009), the first quadrant is essentially in energy equilibrium

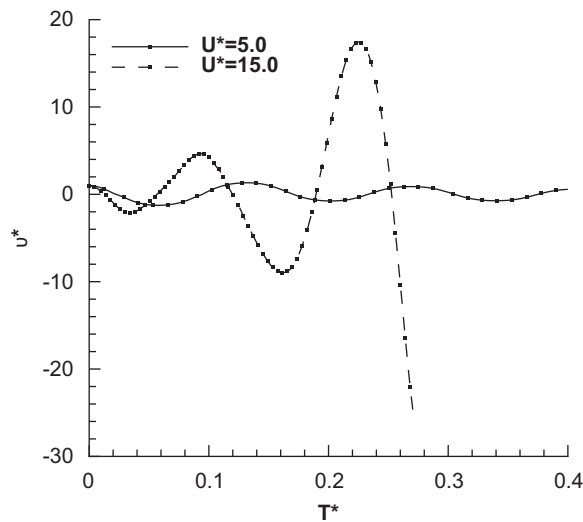


Fig. 4. Plate tip deflection for plate below and above the critical flow velocity.

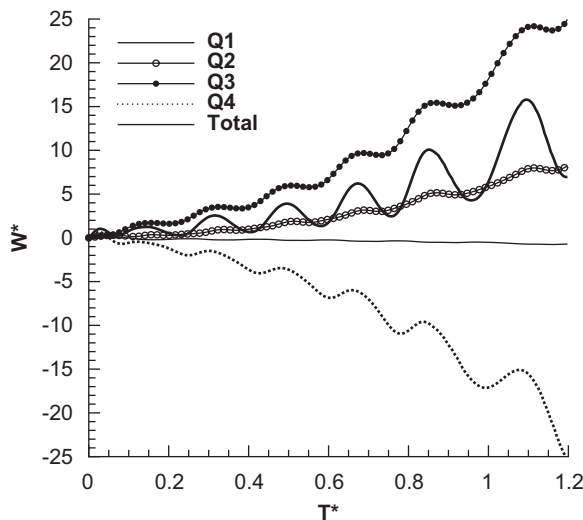


Fig. 5. Work on each quadrant of the plate and the total work on the plate as a function of non-dimensional time. Q1 is at the leading quarter and Q4 is the trailing quarter. Flow conditions and plate properties are $U^* = 6.0$, $L^* = 1.0$ and $C^* = 0.0$.

Table 1
Summary of grid and temporal convergence studies.

Case	NTP	φ	NX_{CFD}	NY_{CFD}
1	4	0.5	160	80
2	8	0.5	320	160
3	16	0.5	640	320
4	8	0.25	320	160
5	8	0.5	320	160
6	8	1.0	320	160

with very little net energy gain or loss compared to the other three quadrants. Energy is transferred to the plate from the fluid in the second and third quadrants of the plate. The rate of energy transfer to the plate in the third quadrant is greater than the rate of energy transfer in the second quadrant. Also consistent with the findings of Howell et al. (2009), plate energy is transferred to the fluid in the trailing quadrant.

To investigate grid and temporal independence of the solution, a deflected plate is released from rest in initially quiescent fluid. The initial plate configuration is first mode deflection with tip displacement equal to $5h$. To characterize the spatial convergence of the solution, the parameter $NTP = h NY_{CFD}/H_{CFD}$ is introduced where NY_{CFD} is the number of nodes in the y direction of the fluid domain and H_{CFD} is the size of the fluid domain in the y direction. The grid and coupling time step parameters for the convergence studies are summarized in Table 1 where NX_{CFD} is the number of nodes in the x direction of the fluid domain. The plate properties for all studies were $\rho_p h = 0.195 \text{ kg/m}^2$, $B = 0.511 \text{ N m}$, $C = 0 \text{ kg/m}^2 \text{ s}$ and $L = 0.1 \text{ m}$. Results of the spatial and temporal convergence studies are presented in Fig. 6 for $NTP = 4, 8$ and 16 and for φ from Eq. (11) set to $0.25, 0.5$ and 1.0 , where $E^* \equiv E_t/E_t(0)$. As shown, the simulation results are grid independent for $NTP \geq 8$ and for $\varphi \leq 0.5$ therefore these values are used for all remaining cases in the study.

4.2. Isolated plate in flow

Fig. 7 shows instantaneous snap shots of the vorticity field around the plate during a typical flapping cycle at (a) 3 ms, (b) 21 ms (c) 28 ms and (d) 31 ms for super-critical flow conditions of $U^* = 15$ and with plate parameters of $L^* = 0.6$ and $C^* = 0.0$ (undamped). The period of one flutter cycle is approximately 16 ms. Early in time, a steady attached viscous boundary layer develops around the plate with a Karman vortex street type wake (Fig. 7(a)). Since at the early stages of flutter the flow is attached over the length of the plate, potential flow characteristics dominate the fluid loading. As the plate motion evolves, separation occurs in the mid plate region, shown in Fig. 7(b), creating an unsteady wake which is dominated by plate motion. With increasing time, deflection amplitude grows and the separation distance of the boundary layer from the plate increases when the plate surface is concave (Fig. 7(c) and (d)); flow separation on the convex side occurs at approximately three-quarters of the plate length. Large vortices are generated at the trailing edge due to the high rate of deflection of the plate tip.

One of the outstanding issues in the understanding and design of flutter energy harvesters is identification of locations on the plate where energy is transferred to or from the fluid. Previous studies have shown that for relatively short plates with $0.5 \leq L^* \leq 1.0$, the vibrations are dominantly second mode and are driven by a phase shift in velocity and pressure which results in energy transfer to the plate in the middle of two quarters (Howell et al., 2009). It has also been conclusively shown that even at supercritical flow conditions, plate energy is dissipated at the trailing edge of the plate (Howell et al., 2009; Tang and Paidoussis, 2008), likely as a result of the unsteady wake induced by plate motion (Huang, 1995); the influence of the wake decreases as L^* increases. To facilitate design of flutter mills, it would be useful to have a parameter which characterizes the local energy transfer based on the plate geometry. Recently, Tang et al. (2009) suggested that the transfer of energy may be correlated with local surface curvature, that is defined as (Stewart, 2004)

$$\kappa = \frac{v''}{(1+v'^2)^{3/2}}, \quad (12)$$

where concave down and up are designated as negative and positive curvatures, respectively. To explore the correlation of power with curvature, Fig. 8 presents a phase plot of the instantaneous non-dimensional power, $\dot{W}^* \equiv \dot{W}L^2/(\rho_p U_\infty^3 h^3)$, versus κ . Consistent with studies (Howell et al., 2009; Tang et al., 2009), maximum instantaneous power loss is observed for values of curvature near zero corresponding to the trailing edge of the plate where the boundary condition $v'' = 0 \text{ m}^{-1}$ is enforced. Two peak instantaneous power regions or lobes centered around $\kappa = -20 \text{ m}^{-1}$ and 40 m^{-1} are visible. The origin of the lobes can be determined by the inset plots in Fig. 7 showing the instantaneous distribution of \dot{W}^* versus κ along the length of the plate. As shown in Fig. 7(b) and (c) the maximum energy transfer to the plate occurs when the tip displacement is at its maximum. As the tip displacement passes through zero, energy is lost from the plate to the fluid over much of the surface (Fig. 7(a) and (d)).

In an effort to uniquely relate energy transfer to the changes in local geometry, the data from Fig. 8 is further sorted using the instantaneous local deflection rate, \dot{v} . Fig. 9 shows a subset of the data for (a) $\dot{v} \geq 0 \text{ m/s}$ and (b) $\dot{v} < 0 \text{ m/s}$. These plots clearly reveal a strong correlation between the instantaneous, local deflection rate and curvature. Energy is

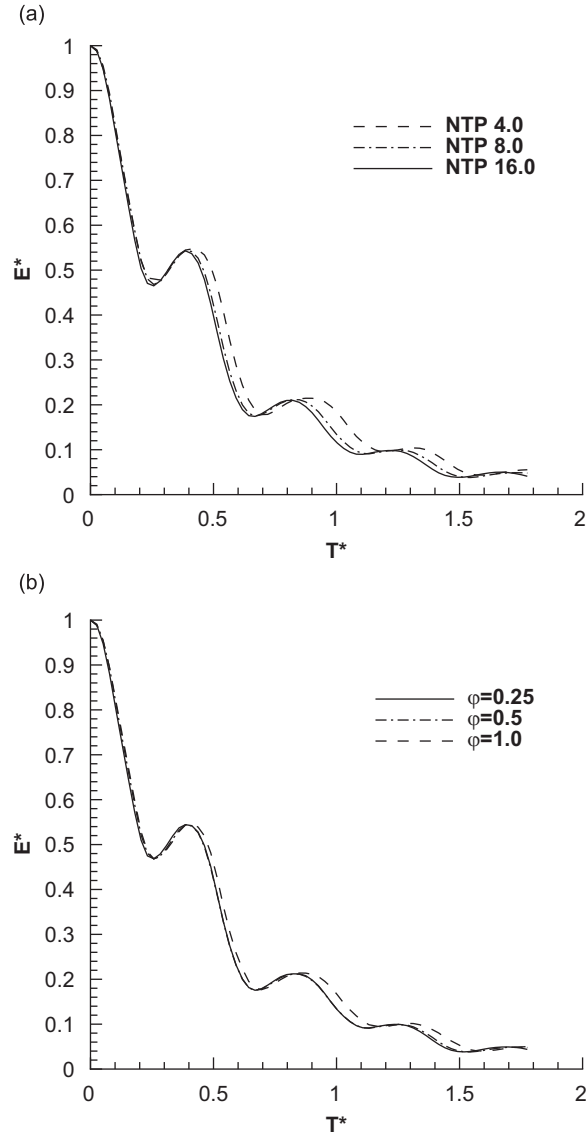


Fig. 6. Non-dimensional energy versus time showing solution convergence with increasing (a) mesh resolution and (b) coupling frequency.

transferred to the plate when either $\kappa < 0 \text{ m}^{-1}$ and $\dot{v} > 0 \text{ m/s}$ or $\kappa > 0 \text{ m}^{-1}$ and $\dot{v} < 0 \text{ m/s}$. Based on these observations, a new curvature-deflection-rate (CDR) metric is defined that is the negative of the product of curvature and displacement rate:

$$\text{CDR} \equiv -\kappa \frac{\dot{v}}{|\dot{v}|}. \tag{13}$$

When $\text{CDR} > 0 \text{ m}^{-1}$ the local lift force is aligned with the direction of plate motion resulting in energy transfer from the fluid to the plate. Fig. 10 shows the same data given in Fig. 8 plotted against CDR where most of the data for positive power production occurs for values of $\text{CDR} > 0 \text{ m}^{-1}$. To quantify the extent of correlation of \dot{W}^* with the newly defined CDR parameter, correlation probabilities (P) are defined for both the positive and negative exchanges of power, $P^{+/-} = N^{+/-} / N_T^{+/-}$, where $N_T^{+/-}$ are the total number of samples for which either $\dot{W}^* > 0$ or $\dot{W}^* < 0$, respectively. The quantity N^+ is the total number of samples for which $\dot{W}^* > 0$ and $\text{CDR} > 0 \text{ m}^{-1}$. The quantity N^- is the total number of samples for which $\dot{W}^* < 0$ and $\text{CDR} < 0 \text{ m}^{-1}$. A perfect correlation corresponds to $P=1$. For the plate at supercritical flow conditions given in Fig. 8, probabilities of $P^+ = 0.83$ and $P^- = 0.48$ are determined—indicating that the CDR parameter is well correlated with regions where power is transmitted to the plate but less so for regions where power is transmitted to the fluid.

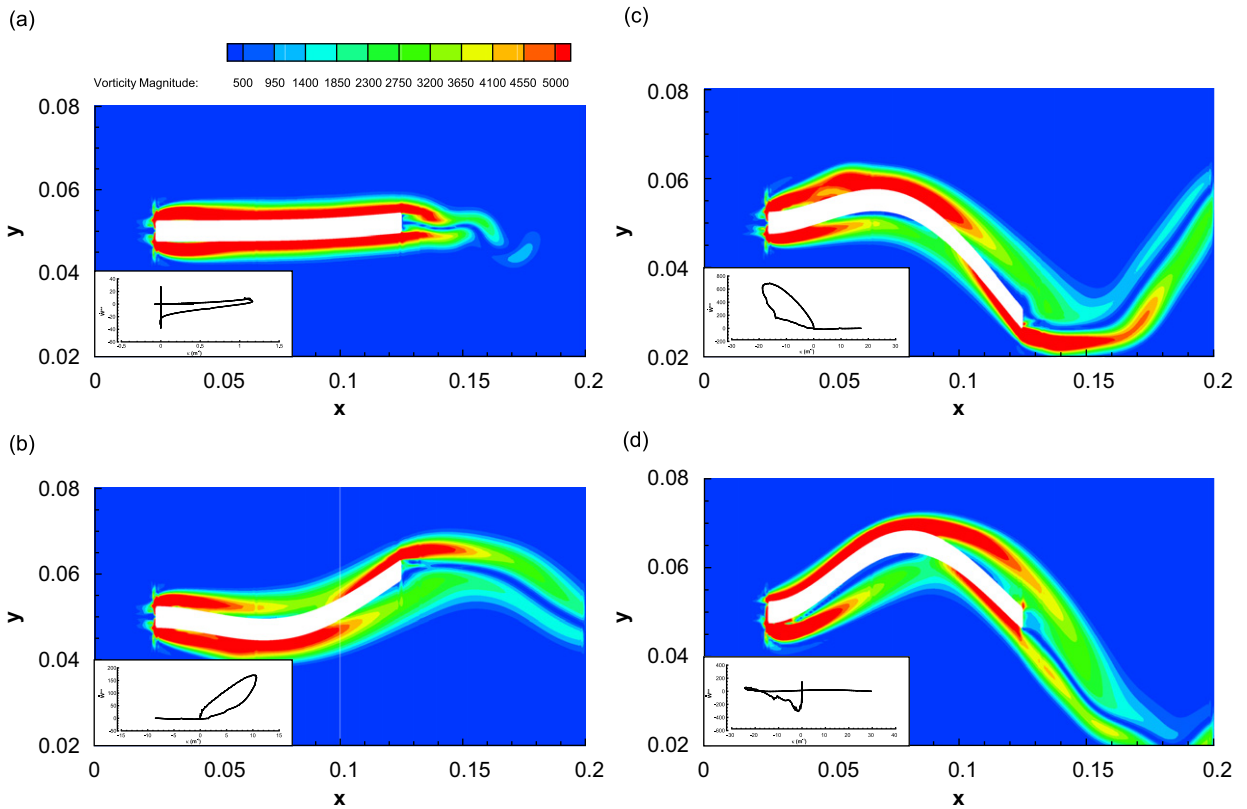


Fig. 7. Instantaneous snapshots of vorticity around plate in supercritical flow at times of (a) 3 ms, (b) 21 ms, (c) 28 ms and (d) 31 ms. Snap shots (b) and (c) are taken at the instant of maximum tip deflection. Flow and plate parameters are $L^* = 0.6$, $U^* = 15.0$ and $C^* = 0$.

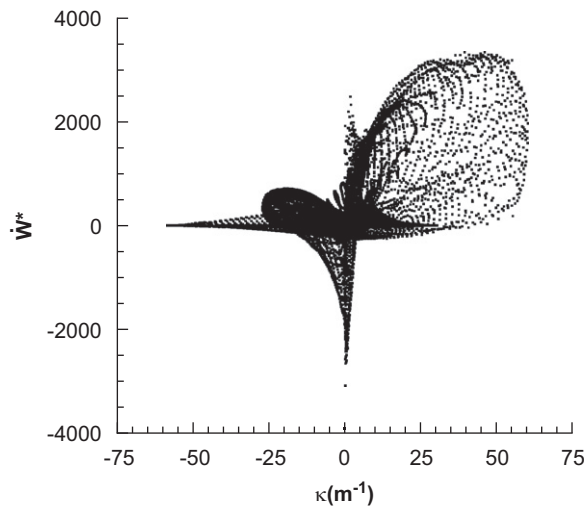


Fig. 8. Phase plot of instantaneous power as a function of local curvature.

To further explore the generality of the CDR parameter, a plate in steady-state flutter is examined by adding dissipation to the plate model. Fig. 11 shows the tip displacement as a function of time for a plate-flow configuration with $C^* = 32.05$, $L^* = 0.6$ and $U^* = 15$ where steady-state vibrations are observed. Plots of instantaneous power as a function of curvature and CDR are shown in Fig. 12(a) and (b), respectively. With the viscous dissipation model, the plate acts as a constant energy sink—continuously absorbing energy from the flow. The positive and negative probabilities of $P^+ = 0.84$ and $P^- = 0.45$, indicating that same level of correlation for the steady-state fluctuations as for the unstable fluttering plate. A more careful examination of the data indicates that samples that do not correlate well for positive power states are

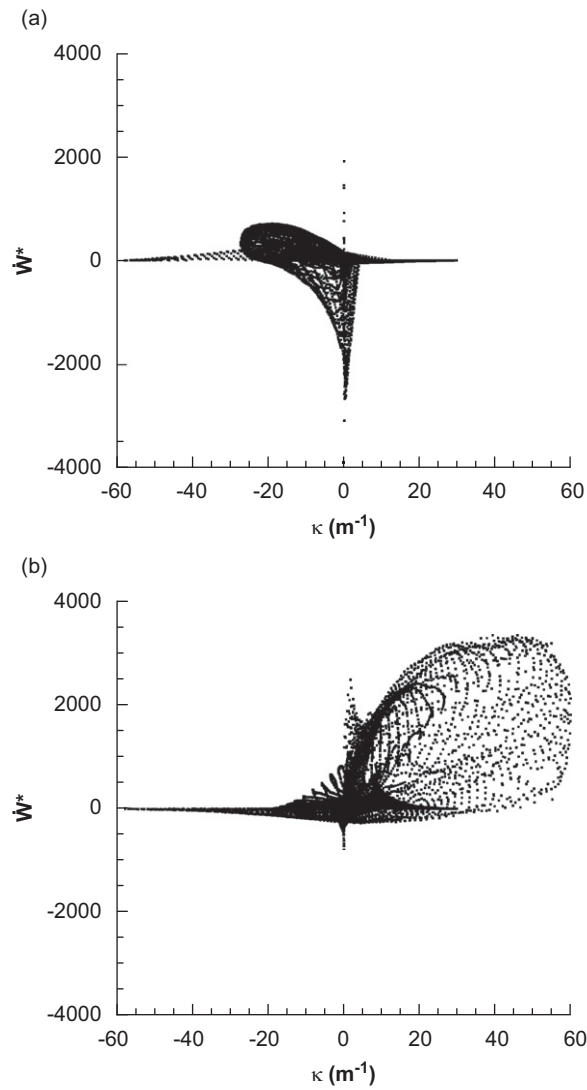


Fig. 9. Phase plot of instantaneous power as a function of local curvature including only points at which (a) $\dot{\psi} > 0$ m/s and (b) $\dot{\psi} < 0$ m/s.

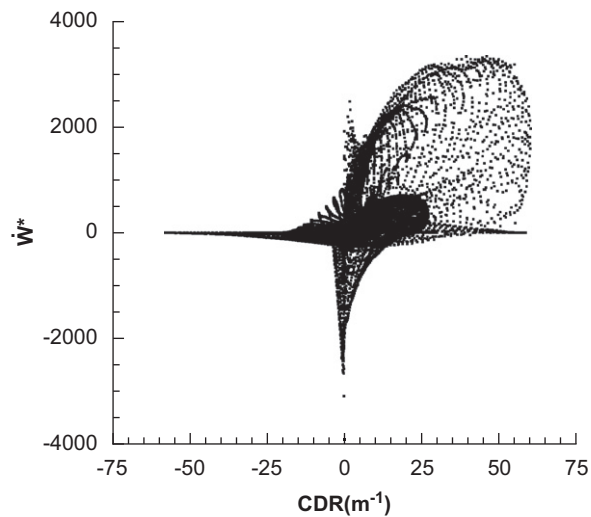


Fig. 10. Phase plot of the instantaneous power as a function of CDR for plate at supercritical flow conditions.

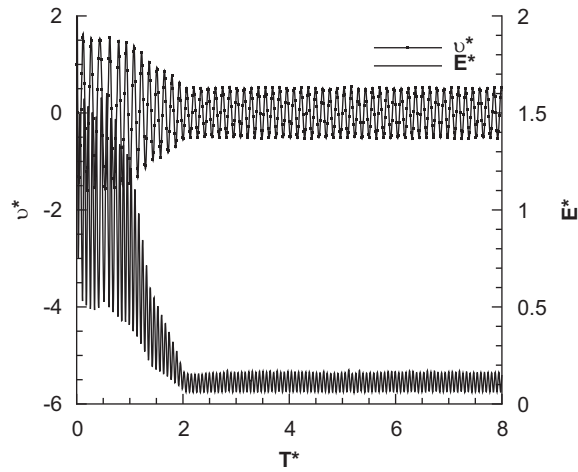


Fig. 11. Tip deflection time history for plate with viscous damping at supercritical flow conditions.

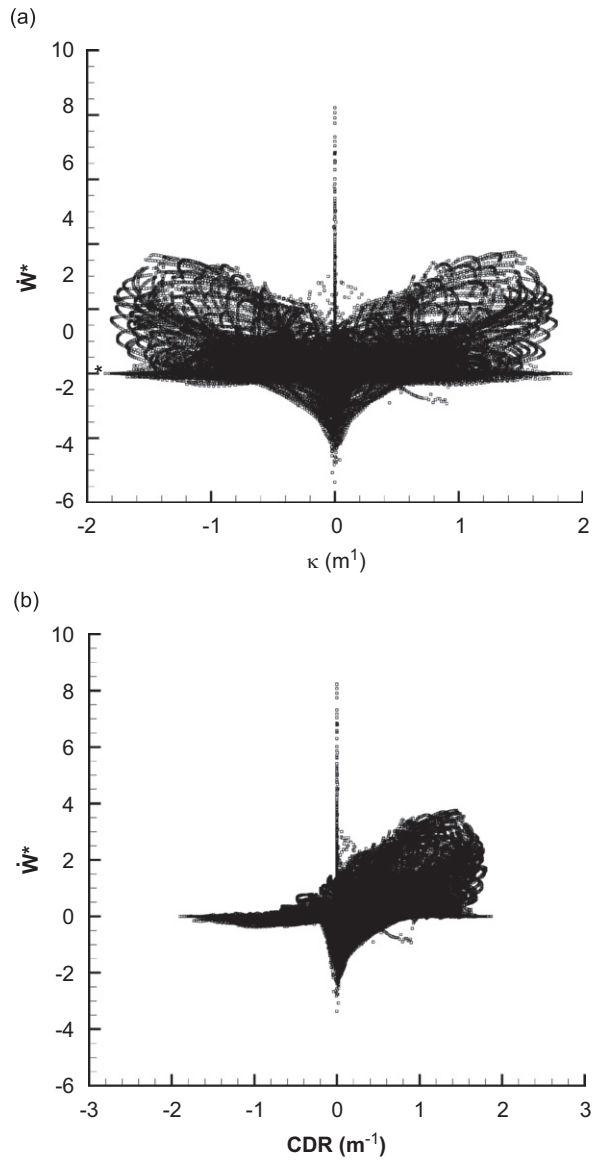


Fig. 12. Phase plots of the instantaneous power versus (a) curvature and (b) CDR for a plate with viscous damping at supercritical flow conditions.

associated with relatively low levels of power. To eliminate these points, a threshold cut-off value of $\dot{W}^* > 0.3\dot{W}_{\max}^*$ is considered, where \dot{W}_{\max}^* is the maximum power observed at the curvature extrema. Using the conditioned data, the revised probability $P^+ = 0.95$ is determined—indicating a very strong correlation of power production with CDR for higher values of \dot{W}^* . It is worth noting that enforcing the threshold cut-off value was not found to have any significant effect on P^- .

4.3. Plate in flow with leading edge bluff body

Several additional cases are conducted with a flow configuration illustrated in Fig. 1. Plate properties were held constant at sub-critical conditions, $U^* = 5.0$, $L^* = 0.6$ and $C^* = 0.0$ while varying the diameter of the leading edge cylinder. Fig. 13 presents the time histories of the normalized tip displacement $v^{**} = v/D$, and energy $E^{**} = E_t L / \rho_p U_\infty^2 h^3$, for the first four cases in Table 2. In the two cases of largest leading edge bluff body, $D/L = 0.67$ and $D/L = 0.5$, the plate develops

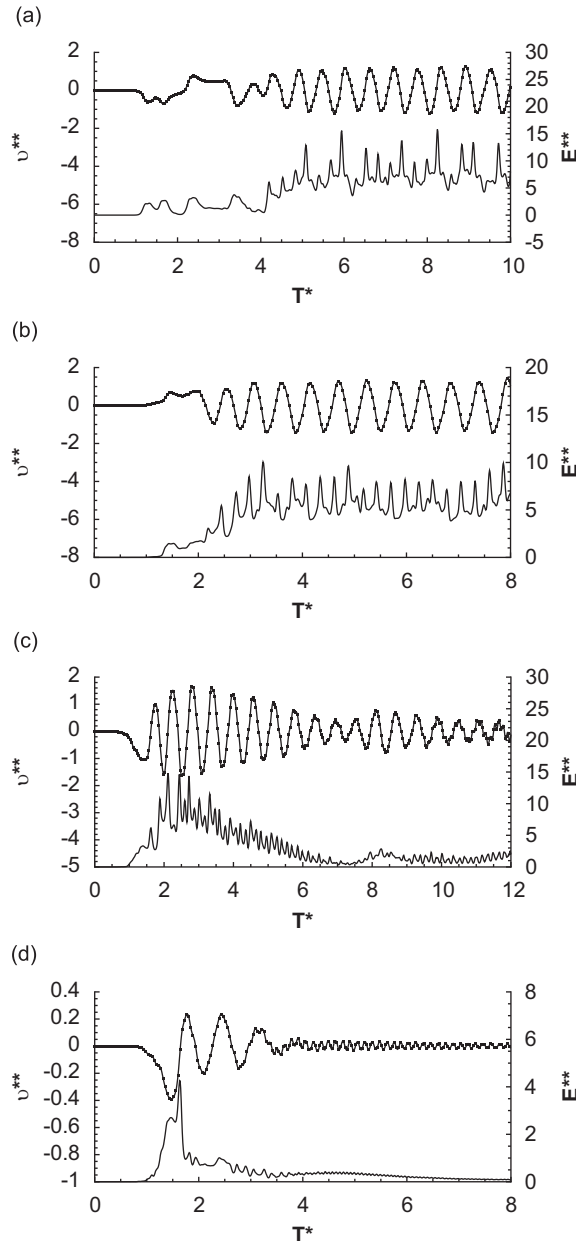


Fig. 13. Time history of deflection (solid line with symbols) and energy (solid line without symbols) for D/L equal to (a) 0.67, (b) 0.5, (c) 0.2 and (d) 0.1. $L^* = 0.6$, $U^* = 5.0$, $C^* = 0.0$ for all cases.

Table 2
Summary of probability correlations as a function of size ratio, D/L .

D/L	L^*	U^*	C^*	P^+	P^-
0.67	0.6	5.0	0.00	0.82	0.66
0.50	0.6	5.0	0.00	0.88	0.71
0.20	0.6	5.0	0.00	–	–
0.10	0.6	5.0	0.00	–	–
0.05	0.6	15.0	0.00	0.83	0.48
0.05	0.6	15.0	32.05	0.84	0.45

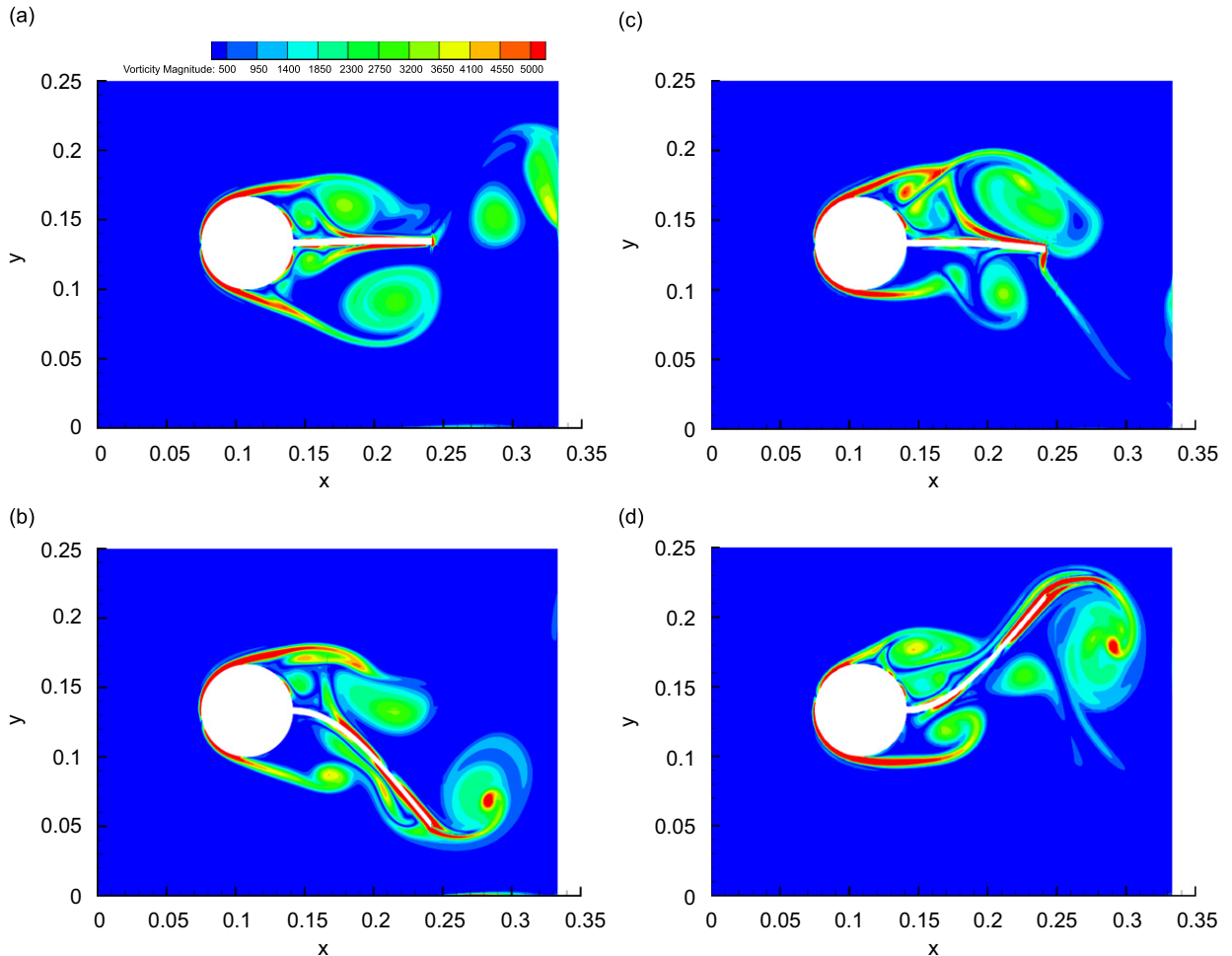


Fig. 14. Vorticity contours with size ratio $D/L = 0.67$ at (a) 330 ms (b) 336 ms (c) 342 ms (d) 347 ms. Flow parameters are same as Fig. 13.

sustained vibrations even though the flow conditions are sub-critical. For the flow configuration with $D/L = 0.1$ and 0.2 , large initial perturbations transition to decaying, small amplitude, high frequency oscillations. The high-amplitude initial perturbations shown in Fig. 13(c) and (d) are dominantly first mode-shape deflections, while the small-amplitude decaying oscillations are primarily second mode.

Fig. 14 shows vorticity contour snapshots around the cylinder and plate for $D/L = 0.67$ at (a) 323 ms, (b) 330 ms, (c) 336 ms and (d) 342 ms. The period of vibration is approximately 25 ms. Fig. 14(a) shows the plate nearly undeflected along the cylinder centerline with downward momentum and a coherent vortex developing on the top side of the plate while a vortex has just been shed from the lower surface. As the plate deflects downward (Fig. 14(b)) it intersects the shed vortex which is being convected downstream. Downwash from the plate and acceleration of the free stream around the plate tip carry the vortex downstream. When the plate moves outside the cylinder's wake, the impinging free stream flow dissipates kinetic energy from the plate until it comes to a halt and reverses direction at which point the favorable pressure gradient results in fluid-to-plate energy transfer. In Fig. 14(c), the plate passes through the cylinder centerline

again as the upper vortex begins to shed. Finally, in Fig. 14(d) the plate tip again deflects outside the wake of the cylinder where it is brought to a halt by the incoming flow.

Table 2 presents the positive and negative correlation probabilities for these cases along with those without a leading edge bluff body (last two cases). Interestingly, the probability correlations for the bluff body flutter cases are as good as those with just the isolated plate with $P^+ = 0.82$ and 0.88 for $D/L = 0.67$ and $D/L = 0.5$, respectively. Probabilities for $D/L = 0.20$ and 0.10 are not provided since the plate does not achieve sustained flutter and simply decays for those cases. For all cases, fluid-to-plate energy transfer is better correlated with positive values of CDR than plate-to-fluid energy transfer with negative values of CDR.

5. Conclusions

A fully coupled, viscous flow, numerical model of a flutter wind energy harvester is developed consisting of a flexible plate in axial flow with and without a leading edge bluff body. Several cases are presented to validate both the plate model and the immersed interface method used for this class of problems. Isolated cantilevered plates in both sub-critical and supercritical flows are explored with and without bluff bodies. For beams in sub-critical flow conditions, it is found that periodic vibrations can be sustained by introducing a sufficiently large bluff body at the leading edge of the plate. A strong correlation between local power production on the plate and a newly introduced curvature-deflection-rate (CDR) metric is established. High probability correlations are computed indicating the usefulness of CDR for determining local power generation with geometry curvature and deflection rate. This parameter could potentially be used in further design of these devices and exploring more generalized plate shapes in order to optimize energy transfer.

Acknowledgments

This research was supported by the Office of Naval Research under Grants N00014-06-1-0623 and N00014-08-C-0591 and by the National Science Foundation (NSF) under Grant CBET-1033328. The authors would also like to thank the University at Buffalo Center for Computation Research (CCR) for providing some of the computing facilities on which the present studies were run.

References

- Arienti, M., Hung, P., Morano, E., Shepherd, J.E., 2003. A level set approach to Eulerian–Lagrangian coupling. *Journal of Computational Physics* 185, 213–251.
- Borazjani, I., Sotiropoulos, F., Ge, L., 2008. Curvilinear immersed boundary method for simulating fluid structure interaction with complex 3d rigid bodies. *Journal of Computational Physics* 227 (16), 7587–7620.
- Crighton, D.G., Oswell, J.E., 1991. Fluid loading with mean flow. i. Response of an elastic plate to localized excitation. *Philosophical Transactions: Physical Sciences and Engineering* 335 (1639), 557–592.
- Desjardin, P.E., O'Hern, T.J., Tieszen, S.R., 2004. Large eddy simulation and experimental measurements of the near-field of a large turbulent helium plume. *Physics of Fluids* 16, 1866–1883.
- Doaré, O., Sauzade, M., Eloy, C., 2011. Flutter of an elastic plate in a channel flow: confinement and finite-size effects. *Journal of Fluids and Structures* 27 (1), 76–88.
- Eloy, C., Souilliez, C., Schouveiler, L., 2007. Flutter of a rectangular plate. *Journal of Fluids and Structures* 23 (6), 904–919.
- Fedkiw, R., 2002. Coupling an Eulerian fluid calculation to a Lagrangian solid calculation with the ghost fluid method. *Journal of Computational Physics* 175, 200–224.
- Fedkiw, R.K., Aslam, T., Merriman, B., Osher, S., 1999. A non-oscillatory Eulerian approach to interfaces in multimaterials flows (the ghost fluid method). *Journal of Computational Physics* 152, 457–492.
- Guo, C., Paidoussis, M., 2000a. Analysis of hydroelastic instabilities of rectangular parallel-plate assemblies. *ASME Journal of Pressure Vessel Technology* 122 (4), 502–508.
- Guo, C., Paidoussis, M., 2000b. Stability of rectangular plates with free side-edges in two-dimensional inviscid channel flow. *ASME Journal of Applied Mechanics* 67 (1), 171–176.
- Howell, R., Lucey, A., Carpenter, P., Pitman, M., 2009. Interaction between a cantilevered-free flexible plate and ideal flow. *Journal of Fluids and Structures* 25 (3), 544–566.
- Howell, R., Lucey, A., Pitman, M., 2011. The effect of inertial inhomogeneity on the flutter of a cantilevered flexible plate. *Journal of Fluids and Structures* 27 (3), 383–393.
- Huang, L., 1995. Flutter of cantilevered plates in axial flow. *Journal of Fluids and Structures* 98 (2), 127–147.
- Humdinger Wind Energy, LLC, 2008. Technical brief of windbelt. See also URL <<http://www.humdingerwind.com>>.
- Inman, D.J., 1996. *Engineering Vibration*. Prentice Hall.
- Kornecki, A., Dowell, E., O'Brien, J., 1976. On the aeroelastic instability of two-dimensional panels in uniform incompressible flow. *Journal of Sound and Vibration* 47 (2), 163–178.
- Li, Y., 1997. Wavenumber-extended high-order upwind-biased finite-difference schemes for convective scalar transport. *Journal of Computational Physics* 133, 235–255.
- Liou, M.-S., 1996. A sequel to AUSM: AUSM+. *Journal of Computational Physics* 129, 364–382.
- Liou, M.-S., 2006. A sequel to ausm, Part ii: Ausm+up for all speeds. *Journal of Computational Physics* 214 (1), 137–170.
- Lucey, A., Balint, T., 2005. Instability of a cantilevered flexible plate in viscous channel flow. *Journal of Fluids and Structures* 20 (7), 893–912.
- Ly, K., Chasteau, V., 1981. Experiments on an oscillating aerofoil and applications to wind-energy converters. *Journal of Energy* 5 (2), 116–121.
- McGurn, M., Ruggirello, K., Desjardin, P.E. A 3d Eulerian–Lagrangian immersed interface method for simulating burning and moving solids. *Journal of Computational Physics*, in review.
- McKinney, W., DeLaurier, J., 1981. Wingmill: an oscillating-wing windmill. *Journal of Energy* 5 (2), 109–115.
- Osher, S., Fedkiw, R., 2003. *Level Set Methods and Dynamic Implicit Surfaces*. Springer, New York.

- Pennington, S., Bauge, T., Murray, B., 2009. Integrity-checking framework: an in-situ testing and validation framework for wireless sensor and actuator networks. In: 2009 Third International Conference on Sensor Technologies and Applications (SENSORCOMM), pp. 575–579.
- Rayleigh, L., 1878. On the instability of jets. *Proceedings of the London Mathematical Society* s1-10 (1), 4–13.
- Reddy, J.N., 1993. *Finite Element Method*. McGraw Hill, New York, NY.
- Sambasivan, S.K., UdayKumar, H., 2009. Ghost fluid method for strong shock interaction part 2: immersed solid boundaries. *AIAA Journal* 47 (12).
- Semler, C., Li, G., Paidoussis, M., 1994. The non-linear equations of motion of pipes conveying fluid. *Journal of Sound and Vibration* 169 (5), 577–599.
- Shafi, A., Manzoor, J., 2009. Toward efficient shared memory communication in MPJ express. In: *IEEE International Parallel and Distributed Processing Symposium*, May.
- Smits, A.J., 1999. *A Physical Introduction to Fluid Mechanics*, 1st ed. John Wiley & Sons.
- Stewart, J., 2004. *Multi-Variable Calculus*, 5th ed. Thomas Learning.
- Tang, L., Paidoussis, M., 2007. On the instability and the post-critical behaviour of two-dimensional cantilevered flexible plates in axial flow. *Journal of Sound and Vibration* 305 (1–2), 97–115.
- Tang, L., Paidoussis, M., 2008. The influence of the wake on the stability of cantilevered flexible plates in axial flow. *Journal of Sound and Vibration* 310 (3), 512–526.
- Tang, L., Paidoussis, M., Jiang, J., 2009. Cantilevered flexible plates in axial flow: energy transfer and the concept of flutter-mill. *Journal of Sound and Vibration* 326 (1–2), 263–276.
- Taylor, G.W., Burns, J.R., Kammann, S.M., Powers, W.B., Welsh, T.R., 2001. The energy harvesting eel: a small subsurface ocean/river power generator. *IEEE Journal of Oceanic Engineering* 26 (4), 539–547.
- Tseng, Y., Ferziger, J.H., 2003. A ghost-cell immersed boundary method for flow in complex geometry. *Journal of Computational Physics* 192, 593–623.
- Wag, C., Tang, H., Liu, T., 2008. An adaptive ghost fluid finite volume method for compressible gas–water simulations. *Journal of Computational Physics* 227, 6385–6409.
- Watanabe, Y., Isogai, K., Suzuki, S., Sugihara, M., 2002. A theoretical study of paper flutter. *Journal of Fluids and Structures* 16 (4), 543–560.
- Xu, S., Aslam, T., Stewart, D.S., 1997. High resolution numerical simulation of ideal and non-ideal compressible reacting flows with embedded internal boundaries. *Combustion Theory and Modelling* 1, 113–142.
- Yadykin, Y., Tenetov, V., Levin, D., 2001. The flow-induced vibration of a flexible strip hanging vertically in a parallel flow, Part 1: temporal aeroelastic instability. *Journal of Fluids and Structures* 15, 1167–1185.
- Ye, T., Mittal, R., Udaykumar, H., Shyy, W., 1999. An accurate Cartesian grid method for viscous incompressible flows with complex immersed boundaries. *Journal of Computational Physics* 156 (2), 209–240.
- Zhu, L., Peskin, C., 2002. Simulation of a flapping flexible filament in a flowing soap film by the immersed boundary method. *Journal of Computational Physics* 179 (2), 452–468.